Partial positive refraction in asymmetric Veselago lenses of uniaxially strained graphene

Y. Betancur-Ocampo*

Instituto de Ciencias Físicas, Universidad Nacional Autónoma de México, 62210 Cuernavaca, México

(Received 16 July 2018; revised manuscript received 10 October 2018; published 26 November 2018)

Asymmetric Veselago lenses (AVLs) can be created from ballistic p-n and n-p-n homojunctions of uniaxially strained graphene. This atypical converging electron flow emerges by applying uniaxial tension out of the device's symmetry axes. Part of the electron flow needs to be positively refracted to focus on an asymmetric spot, whose location is tunable with the strain. In AVLs, Klein tunneling is angularly shifted with regard to the normal incidence. This perfect transmission occurs in the straight line that connects the point source and focus, which is unaffected by variation of the Fermi level and voltage gate. Moreover, the mirror symmetry breaking by the strain also causes the asymmetry in Fabry-Pérot interference. The novel electron optical laws allow us to evidence that reflected and refracted electrons in AVLs lie on the same straight line with opposite group velocities and pseudospins. Unlike isotropic graphene, electrons under normal incidence present backscattering, angles of reflection, and refraction different from zero. The average particle transmission is higher (lower) than the isotropic case when the tensile strain is increased near (far away from) the normal direction. These results may be useful for designing strain-bendable probing tips in scanning tunneling microscopes.

DOI: 10.1103/PhysRevB.98.205421

I. INTRODUCTION

Electron optics offers the opportunity to manipulate the trajectories of electrons for concrete applications in nanoelectronics [1–19]. Ballistic charge carriers crossing an interface, which separates regions with different doping levels, can simulate refraction phenomena such as the light across inhomogeneous media [1,2]. Recently, graphene bipolar n-p-n junctions have served as a platform for the realization of outstanding optical-like phenomena in condensed matter, such as Klein tunneling (KT) and Fabry-Pérot (FP) oscillations [20–28]. Negative refraction of massless Dirac fermions was predicted and tested without and in the presence of a uniform magnetic field [28–32]. The pseudorelativistic nature of electrons makes it more feasible to realize electron optics in Dirac materials than conventional semiconductors [30]. These recent and special features in electron optics pave the way for the use of superlenses to manipulate electron flow such as the light in metamaterials [3,33–36]. On the other hand, strain engineering in graphene has opened a wide range of possibilities to control the electronic and transport properties [37–40]. Currently, the study of strain effects on the electronic band structure in graphene is considered in order to modulate physical properties [40,41]. A tentative merging of these research topics may provide a broad perspective to investigate novel and unusual transport effects in graphene and other Dirac materials.

Many contributions in strained graphene are dedicated to the control of valley spin polarization, where the main motivation is to use the valley degree of freedom as a conveyor of quantum information [13,42,43]. This proposal arises due to the valley dependence of refraction when electrons tunnel from unstrained to strained graphene regions [44–48]. However, obtaining well-defined isotropic and anisotropic graphene regions is difficult in practice. While p-n and n-p-n homojunctions of uniaxially strained graphene (USG) are more feasible for testing transport phenomena, they have been scarcely addressed due to the valley independence in the electron transport. Nevertheless, unusual optical-like phenomena emerge considering fully strained graphene sheets. In this work we show that in-plane deformation out of the symmetry axes of a graphene p-n junction creates asymmetric Veselago lenses (AVLs). Different from those perfect lenses in metamaterials and isotropic graphene, which focus the particle flow towards a symmetric spot [3], strained graphene homojunctions can bend the converged electron flow. Thus, part of the electron flow is positively refracted to focus on an asymmetric spot. In these systems, reflected and refracted electrons have inverted pseudospins and move in opposite directions. Further, the KT is angularly shifted and occurs at the straight line that links the point source and focus. The particle transmission efficiency in AVLs is higher (lower) than in the unstrained case when the tensile strain is increased near (far away from) the normal direction. Since the FP interference of n-p-n homojunctions do not have mirror symmetry, resonant tunneling under normal incidence appears. Such results may be useful for designing an improved scanning tunneling microscope with a bendable probing tip.

This paper is organized as follows: in Sec. II the tight-binding (TB) approach to nearest neighbors for an anisotropic graphene sheet is used. In this calculation the uniaxial strain modifies the electronic band structure changing the rotation and shape of the Dirac cones. An effective TB Hamiltonian is obtained through Taylor expansion around the Dirac points up to first order in the wave vector. Thus, the complex velocity parameters of the Weyl-like Hamiltonian are expressed in terms of uniaxial strain components. Section III establishes the reflection and refraction laws of electrons impinging the interface of homojunctions. The application of these novel

*ybetancur@icf.unam.mx

electron optics laws in Sec. IV evidences how partial positive refraction of a particle flow favors the creation of AVLs. Section IV also shows the angular deviation of KT and average particle transmission efficiency. The shifting of FP fringes of USG bipolar n-p-n homojunctions are discussed in Sec. V. Conclusions and final remarks are made in Sec. VI.

II. COMPLEX VELOCITIES AND THE EFFECTIVE TB WEYL-LIKE HAMILTONIAN OF UNIAXIALLY STRAINED GRAPHENE

USG is constituted by two deformed triangular Bravais sublattices which are labeled A and B [see Fig. 1(a)]. This deformed crystal possesses a unit cell having two carbon atoms with decoupled p_z and σ orbitals. The atomic sites are displaced by applying the tension T in the direction ζ. The Cartesian system is set with the x axis along the ZZ bond in the unstrained configuration [39]. The positions of nearest neighbors are denoted by $\vec{\delta}_1$, $\vec{\delta}_2$, and $\vec{\delta}_3$ on the underlying sublattice A. The lattice vectors $\vec{a}_1$ and $\vec{a}_2$ and reciprocal ones $\vec{b}_1 = (2\pi/|\vec{a}_1 \times \vec{a}_2|)\vec{a}_2 \times \hat{z}$ and $\vec{b}_2 = (2\pi/|\vec{a}_1 \times \vec{a}_2|)\hat{z} \times \vec{a}_1$ build the whole positions in the deformed hexagonal lattices, where $\hat{x}$, $\hat{y}$, and $\hat{z}$ are unit vectors of the Cartesian system. The first Brillouin zone corresponds to a distorted hexagon with two nonequivalent high-symmetry points, K and K'.

From elasticity theory [39,49–51], the uniaxial strain tensor is written as

$$\mathbf{u} = (p\mathbf{I} + q\mathbf{S})\epsilon, \tag{1}$$

where the constants p and q are defined by $p = (1-\nu)/2$ and $q = (1+\nu)/2$, with ν being the Poisson ratio of graphene [40,51]. The identity matrix $\mathbf{I}$ has dimensions 2×2 as well as $\mathbf{S}$, which is expressed in terms of the Pauli matrices $\mathbf{S} = \sigma_z \cos 2\zeta + \sigma_x \sin 2\zeta$. The tensile strain ϵ in graphene is proportional to the magnitude of tension T [39]. Thus, ϵ is defined for quantifying the percentage of deformation along the ζ direction, as shown in Fig. 1(a). The perpendicular direction is contracted by a quantity of $-\nu\epsilon$. The predicted failure strain occurs for a value of approximately 28% [51,52]. Since $\mathbf{u}$ is a homogeneous strain tensor, the atomic position in the current configuration is given by $\vec{r} = (\mathbf{I} + \mathbf{u})\vec{r}_0$, where $\vec{r}_0$ indicates the sites on the unstrained system. Hence, the deformed lattice vectors

$$\begin{aligned}\vec{a}_1 &= \sqrt{3}a[\hat{x}(1 + p\epsilon + q\epsilon\cos 2\zeta) + \hat{y}q\epsilon \sin 2\zeta],\\ \vec{a}_2 &= \frac{\sqrt{3}}{2}a\{\hat{x}[1 + p\epsilon + 2q\epsilon\cos(2\zeta - \pi/3)]\\ &\quad + \hat{y}[\sqrt{3}(1 + p\epsilon) + 2q\epsilon\sin(2\zeta - \pi/3)]\}\end{aligned} \tag{2}$$

are related to the uniaxial strain parameters, where a is the bond length in pristine graphene [53]. Thus, the relative nearest-neighbor sites for USG $\vec{\delta}_1 = 2\vec{a}_1/3 - \vec{a}_2/3$, $\vec{\delta}_2 = 2\vec{a}_2/3 - \vec{a}_1/3$, and $\vec{\delta}_3 = -\vec{\delta}_1 - \vec{\delta}_2$ are also obtained.

In order to calculate the energy band structure from the TB approach we need to establish the relation of hopping parameters to the uniaxial strain tensor. These TB parameters are the probability amplitudes that an electron in sublattice A hops to neighboring sites. The hoppings can be modeled with the exponential decay rule $t_j = t\exp[-\beta(\delta_j/a - 1)]$, where β is the Grüneisen constant, t is the hopping in pristine graphene, and δ_j are the deformed bond lengths [39,41,53,54]. Thus, the complete relation of t_j as a function of strain parameters is given by

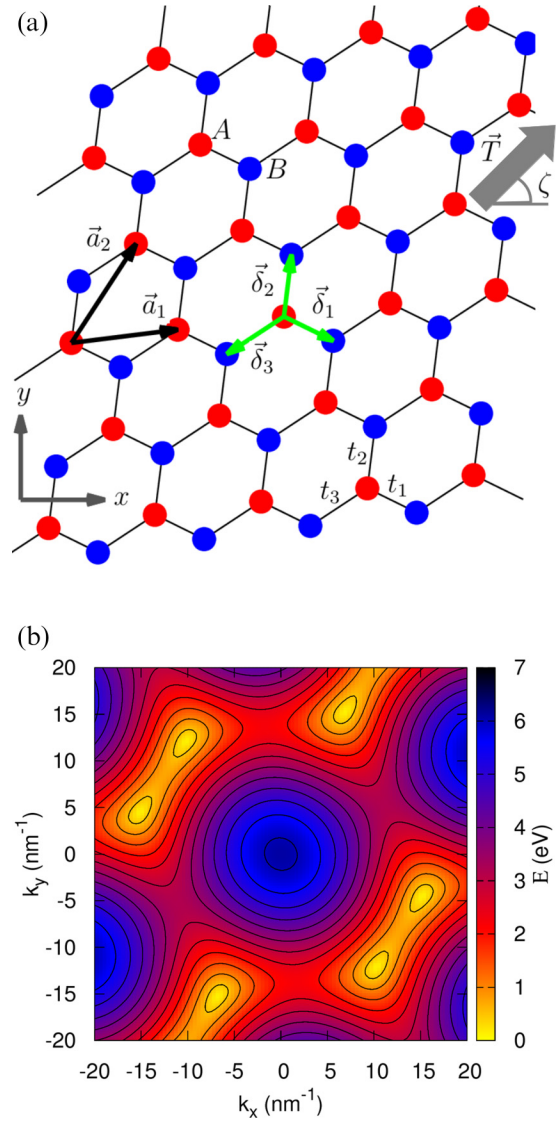

FIG. 1. (a) Schematic representation of uniaxially strained graphene. Red and blue circles correspond to the sites of triangular sublattices A and B, respectively. The x axis matches the zigzag bond in the unstrained case. The uniaxial tension $\vec{T}$ is applied along the ζ direction. The strained configuration has three different nearest-neighbor hopping parameters t_j and bond lengths δ_j. The lattice vectors are denoted by $\vec{a}_1$ and $\vec{a}_2$. (b) Contour energy density near the first Brillouin zone for the conduction band obtained from the TB approach to nearest neighbors using the set of strain values $\epsilon = 23\%$ and $\zeta = 45^\circ$.

$$\delta_j = a\sqrt{\left[1 + p\epsilon + q\epsilon\cos\left(2\zeta + \frac{2j-1}{3}\pi\right)\right]^2 + \epsilon^2 q^2 \sin^2\left(2\zeta + \frac{2j-1}{3}\pi\right)}. \tag{3}$$

Since the overlap terms and the next-nearest-neighbor hopping have a negligible contribution in graphene [55], the TB Hamiltonian is considered only up to nearest neighbors,

$$H_{TB} = \sum_{j=1}^{3} \begin{bmatrix} 0 & t_j e^{i\vec{k}\cdot\vec{\delta}_j} \\ t_j e^{-i\vec{k}\cdot\vec{\delta}_j} & 0 \end{bmatrix}. \tag{4}$$

Therefore, the electronic band structure of USG is obtained from the eigenvalues of the TB Hamiltonian (4),

$$E_{\pm} = s\sqrt{\sum_{i=1}^{3} t_i^2 + 2\sum_{i<j}^{3} t_i t_j \cos[\vec{k}\cdot(\vec{\delta}_i - \vec{\delta}_j)]}, \tag{5}$$

where the band index $s = \mathrm{sgn}(E)$ indicates the valence ($s = -1$) and conduction ($s = 1$) energy bands. The corresponding eigenstates of the Hamiltonian (4) are expressed as $|\Psi(\vec{k})\rangle = \frac{1}{\sqrt{2}}(1, se^{i\phi(\vec{k})})$, where

$$\phi = -\arctan\left(\frac{\sum_j t_j \sin(\vec{k}\cdot\vec{\delta}_j)}{\sum_j t_j \cos(\vec{k}\cdot\vec{\delta}_j)}\right) \tag{6}$$

is the pseudospin angle. The anisotropy induced by the application of uniaxial strain causes the distortion of energy bands, as shown in Fig. 1(b). Contour curves around Dirac points evolve from an elliptical to nontrivial shape when the energy is increased. If TB Hamiltonian (4) is expanded around the Dirac point performing $\vec{k} = \vec{q} + \vec{K}_D$, where the Dirac point position $\vec{K}_D$ satisfies $\sum_j t_j \exp(-i\vec{K}_D\cdot\vec{\delta}_j) = 0$, the effective Weyl-like Hamiltonian

$$H_W = \begin{bmatrix} 0 & w_x^{c*} p_x + w_y^{c*} p_y \\ w_x^c p_x + w_y^c p_y & 0 \end{bmatrix} \tag{7}$$

is expressed in terms of complex velocities $\vec{w}_c$. These velocities are defined as

$$\vec{w}_c = \left(w_x^c, w_y^c\right) = i\sum_{j=1}^{3} \frac{\vec{\delta}_j}{\hbar} t_j e^{-i\vec{K}_D\cdot\vec{\delta}_j}, \tag{8}$$

which establishes a relation to the strain parameters through the lattice vectors and hopping parameters. The Hamiltonian (7) can be changed to the standard form $H_W = v_{ij}\sigma_i p_j$ if the complex velocity components w_x^c and w_y^c are written as $w_x^c = w_x e^{-i\alpha_x}$ and $w_y^c = w_y e^{i\alpha_y}$, where α_x and α_y are the velocity phases. Useful identities of complex velocities with hopping parameters and lattice vectors are shown in Appendix A. On the other hand, a similar form of the Hamiltonian (7) is obtained from the other nonequivalent Dirac point $-\vec{K}_D$. Thus, it is possible to construct a 4×4 block-diagonal matrix representation $H = \tau_z \otimes H_W$, where τ_z is the z component Pauli matrix acting on pseudospin space and discriminating the contribution of the pseudospin valleys [55].

III. OPTICAL LAWS OF MASSLESS DIRAC FERMIONS IN ANISOTROPIC MEDIA

Optical-like phenomena can be simulated from ballistic p-n homojunctions of USG, as shown in Fig. 2(a). The external split-gate structure V and V' creates an abrupt step potential between regions I and II which guarantees the transmission by propagation modes. The necessary conditions for obtaining electron optics require us to lead the system to a ballistic regime [6,18,56]. Such special conditions were recently achieved in the experimental observation of negative refraction of electrons [29,30]. In this device, the linear interface separates two regions with different charge densities (see Fig. 2). Thus, electrons tunnel on the interface, changing their group velocity and pseudospin. This is essentially important for controlling electron flow through the tuning of strain parameters and Fermi level. The point source V_S in Fig. 2(a) injects electrons in a wide angular sector. In order to avoid unwanted interference by multiple reflections at the borders, an extended bias V_D voltage drains the output electrons. When particles impinge on the interface, the optical laws describe the redirection of reflected and refracted flow as well as the scattering probability. The conservation of energy E, linear

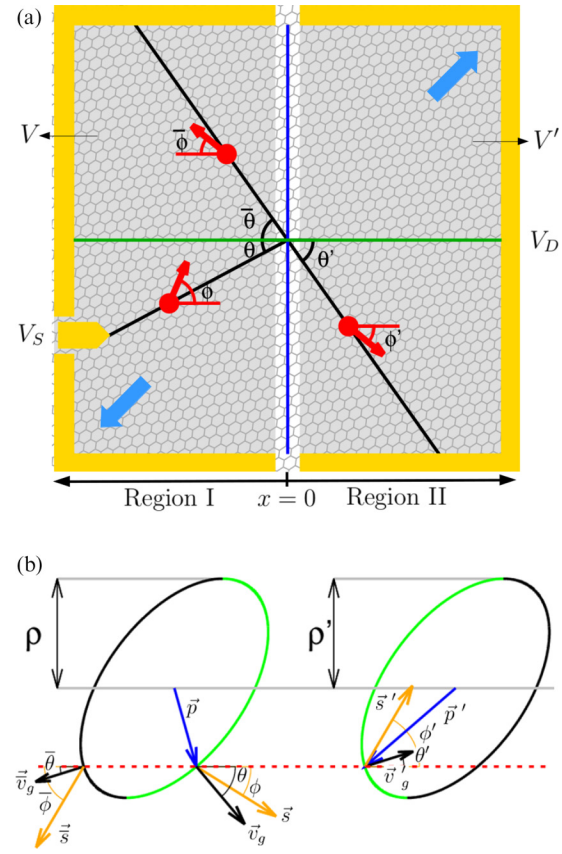

FIG. 2. Geometrical optics convention of angles and kinematical construction in the p-n homojunction of uniaxially strained graphene. (a) An incoming electron beam with angle of incidence θ and pseudospin angle ϕ scatters at the interface (dark blue line) at $x = 0$. Outgoing electron rays with angles of pseudospin $\overline{\phi}$ (ϕ') and reflection $\overline{\theta}$ (refraction θ') obey atypical reflection (refraction) laws (10) and (17) [(11) and (19)], respectively. (b) Kinematical construction shows the scattering of electrons in the reciprocal space. The ellipses correspond to the energy contour at the Fermi level $E = V_0/2$ for both regions. The dashed red line (green semiarcs) represents the conservation of linear momentum p_y (probability current density j_x). Refraction index ρ (ρ') is the vertical half width of the ellipse in region I (II). The black and gold arrows denote the direction of group velocity and pseudospin angles, respectively.

momentum p_y, and probability current density j_x are useful for establishing these electron optics laws in USG, which are schematically represented by the kinematical construction in Fig. 2(b).

The refraction index ρ has a direct geometrical meaning and corresponds to the vertical half width of the elliptical energy contour at the Fermi level [see Fig. 2(b)]. The primed quantities denote region II. It is possible to establish an auxiliary Snell's law through the conservation of p_y given by $\rho \sin\chi = \rho' \sin\chi'$, where χ and χ' are effective angles. Although these quantities differ in the genuine angles of scattering θ and θ', which are given by the group velocity direction, the angles χ are useful for simplifying the optical laws. Using the dispersion relation of Hamiltonian (7), the components of linear momentum can be expressed as $p_x = \pm(w_y/w_x)\rho \sin(\alpha_x + \alpha_y \mp s\chi)$ and $p_y = \rho \sin\chi$ (see Appendix B). The minus in p_x indicates reflection for region I. From geometrical arguments, it is shown that the refraction index is $\rho = |E - V|/[w_y \sin(\alpha_x + \alpha_y)]$. Thus, the definition of pseudospin angle and conservation of p_y allow us to derive the following relations (see Appendix B):

$$\phi = s\chi - \alpha_x, \quad \overline{\phi} = s\chi + \alpha_x, \quad \phi' = s'\chi' - \alpha_x, \tag{9}$$

where the geometrical optics convention for angles is used. The overline denotes the reflected quantities. In standard form, the reflection law of pseudospin for anisotropic massless Dirac fermions is written as

$$\overline{\phi} = \phi + 2\alpha_x. \tag{10}$$

It is worth noting that reflected electron beams do not obey the conventional reflection law $\phi = \overline{\phi}$. This is because uniaxial strain along the ζ direction converts the circular Dirac cone to a rotated elliptical one. The regular expression of this law is restored straining along $\zeta = 0^\circ$ or 90°, where nonrotated elliptical Dirac cones are obtained. On the other hand, Snell's law of pseudospin

$$s\rho \sin(\phi + \alpha_x) = s'\rho' \sin(\phi' + \alpha_x) \tag{11}$$

is also reduced to the conventional form when $\alpha_x = 0$. An important consequence of this novel refraction law reveals that the conservation of pseudospin occurs for $\phi = \phi' = -\alpha_x$ regardless of the Fermi level. Since the group velocity and pseudospin of electrons have different directions in anisotropic systems, perfect transmission emerges in a preferred direction which is not necessarily the normal incidence. In order to confirm this fact the Fresnel-like coefficient is derived using the wave function

$$|\Psi_I\rangle = \frac{1}{\sqrt{2}}\begin{pmatrix} 1 \\ se^{i\phi} \end{pmatrix} e^{ixp_x/\hbar} + \frac{1}{\sqrt{2}} r \begin{pmatrix} 1 \\ -se^{-i\overline{\phi}} \end{pmatrix} e^{-ix\overline{p}_x/\hbar} \tag{12}$$

in region I, where the coefficient r is the probability amplitude for the reflected beam. The state $|\Psi_I\rangle$ takes into account the novel refraction law of pseudospin (10). However, in region II, the transmitted wave function is given by

$$|\Psi_{II}\rangle = \frac{1}{\sqrt{2}} t' \begin{pmatrix} 1 \\ s'e^{i\phi'} \end{pmatrix} e^{ixp'_x/\hbar}, \tag{13}$$

where the amplitude for the transmitted beam is denoted by t'. The probability amplitudes are calculated from the continuity condition for the wave functions (12) and (13) at $x = 0$. Solving the equation system for r and t' and substituting the relations (9), the transmission probability

$$T_{pn}(\chi, \chi') = \frac{\cos\chi \cos\chi'}{\cos^2\left[\frac{1}{2}(s'\chi' + s\chi)\right]} \tag{14}$$

straightforwardly confirms that $\phi = \phi'$ leads to $T(0) = 1$, where $\chi = \chi' = 0$. In order to show that the KT of anisotropic massless Dirac fermions in p-n homojunctions of USG is angularly shifted when $\zeta \neq 0^\circ$ and 90°, the angles of scattering must be related in terms of the effective angles. Thus, the Fresnel-like coefficient of electrons $T(\chi, \chi')$ can be expressed as a function of θ and θ'. The calculation of group velocity serves for finding the angle of incidence θ with χ (see Appendix B)

$$\tan\theta = \pm \frac{w_y \cos[\chi \mp s(\alpha_x + \alpha_y)]}{w_x \cos\chi}. \tag{15}$$

Again the minus sign is for the angle of reflection $\overline{\theta}$. The relation between the angle of refraction θ' and χ' can be obtained by choosing the plus sign and performing the substitutions $\theta \to \theta'$, $\chi \to \chi'$, and $s \to s'$. Since $\chi = \chi' = 0$ in Eq. (14) leads to the prediction of a perfect transmission, the angular shifting of KT

$$\theta_{KT} = \theta'_{KT} = \arctan\left[\frac{w_y}{w_x}\cos(\alpha_x + \alpha_y)\right] \tag{16}$$

is found by setting $\chi = 0$ or $\chi' = 0$ in Eq. (15). It is worth noting that the present result is independent of Fermi level and potential profile. The deviation θ_{KT} can be tuned only by the strain parameters ϵ and ζ, as shown in Fig. 3. For tensile strains along $\zeta = 0^\circ$ and 90°, electrons have perfect transmission under normal incidence. However, the application of tension out of the normal axis deviates the KT path. With values of strain up to 10%, it is possible to observe an angular shifting of the perfect transmission around 10° for a ζ range from approximately 30° to 60°. The direction of tension determines the sign of θ_{KT}. Figure 3 shows that $\theta_{KT}(-\zeta) = -\theta_{KT}(\zeta)$, in accordance with the mirror symmetry operation $y \to -y$.

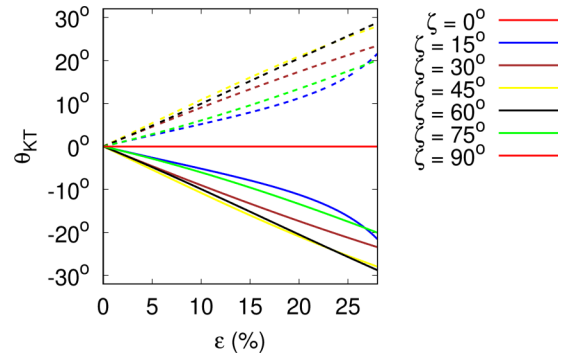

FIG. 3. Angular deviation of Klein tunneling as a function of the strain parameters ϵ and ζ. The dashed curves correspond to the negative values of $\zeta = -15^\circ$ (blue), -30° (brown), -45° (yellow), -60° (black), and -75° (green).

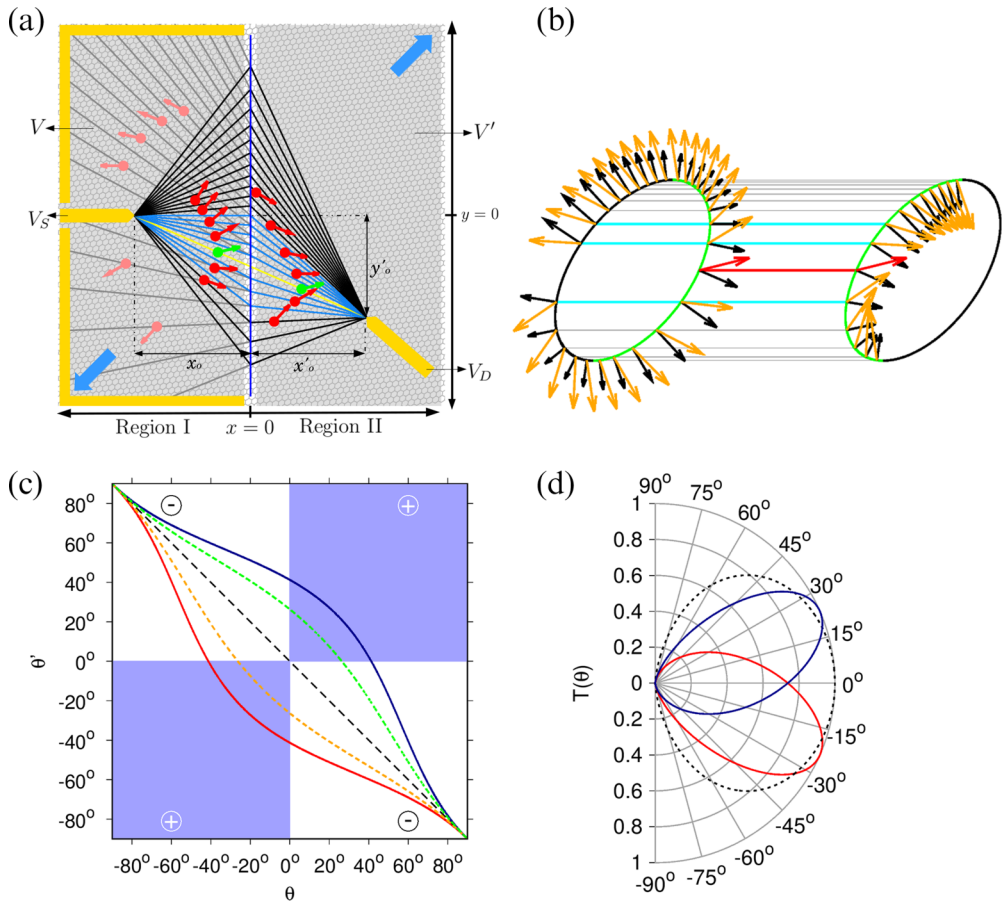

FIG. 4. Partial positive refraction and angular shifting of Klein tunneling in an asymmetric Veselago lens. (a) The special lens can be obtained by applying the tensile strain $\epsilon = 23\%$ along the direction $\zeta = 45^\circ$. When the point source at $(x_0, 0)$ with $x_0 < 0$ spreads electrons towards the interface, the refracted flow meets at the spot $(-x_0, y_0')$ for $E = 50$ meV, $V = 0$, and $V' = V_0 = 100$ meV. The blue rays indicate the beams with positive refraction. The yellow straight line, which links the point source and focus, is the Klein tunneling path with deviation angle $\theta_{KT} = -23.7^\circ$ given by Eq. (16). (b) Kinematical construction reveals how the positive refraction, atypical reflection, and deviation of Klein tunneling emerge. Black (red and gold) arrows correspond to group velocities (pseudospins). Horizontal lines denote the conservation of p_y. The pseudospin and group velocity are conserved for $p_y = 0$ (red line). The turquoise horizontal lines show the positive refraction of group velocity. (c) Angle of refraction θ' as a function of θ for the set of values $\epsilon = 23\%$ and $\zeta = 45^\circ$ (red curve), 15° (dashed orange), 0° (dashed black), -15° (dashed green), and -45° (blue). White and blue regions indicate negative and positive refraction, respectively. (d) Transmission probability as a function of θ for the same set of parameters as in (c). The corresponding $T(\theta)$ for the dashed orange and green curves in (c) are not shown for the sake of clarity.

Another way to write the reflection and refraction laws of electrons in p-n homojunctions of USG is given by

$$\tan\overline{\theta} = \tan\theta - 2\tan\theta_{KT}, \tag{17}$$

$$\tan\theta' = ss'\tan\theta + (1 - ss')\tan\theta_{KT}, \tag{18}$$

where the last expression for the refraction law is obtained from the geometrical condition $\rho = \rho'$, which corresponds to the special case of elliptical energy contours with the same vertical half width at the Fermi level (see Appendix B). It is interesting to note that electrons impinging under normal incidence have nonzero angles of reflection and refraction. Since elliptical Dirac cones are rotated on both sides of the junction the outgoing electron beam has a v_y component different from zero, as shown in Figs. 2(b) and 4(b). The scattering of electrons in p-n homojunctions of USG is discussed in the following section.

IV. ELECTRON TUNNELING IN ASYMMETRIC VESELAGO LENSES

The p-n homojunction of USG satisfying the focusing condition leads to the appearance of an AVL, as shown in Fig. 4(a). If tensile strain is applied along the $\zeta \neq 0^\circ$ and 90° direction, the Dirac cones rotate. This rotation makes the converged electron flow asymmetric. Therefore, the focus is moved out of the normal axis [see Fig. 4(a)]. Thus, a divergent flow emitted at $(x_0, 0)$ with $x_0 < 0$ in region I is focused on the spot (x_0', y_0'). The geometrical relation between θ and θ' of AVLs can be obtained from the ray equations $y_I = (x - x_0)\tan\theta$ and $y_{II} = x\tan\theta' - x_0\tan\theta$ for regions I and II, respectively. The specific relationship $\tan\theta' = \frac{x_0}{x_0'}\tan\theta - \frac{y_0'}{x_0}$ is identical to Snell's law in Eq. (18). In this way, the position of focus $x_0' = -x_0$ and $y_0' = -2x_0\tan\theta_{KT}$ is a function of the strain parameters.

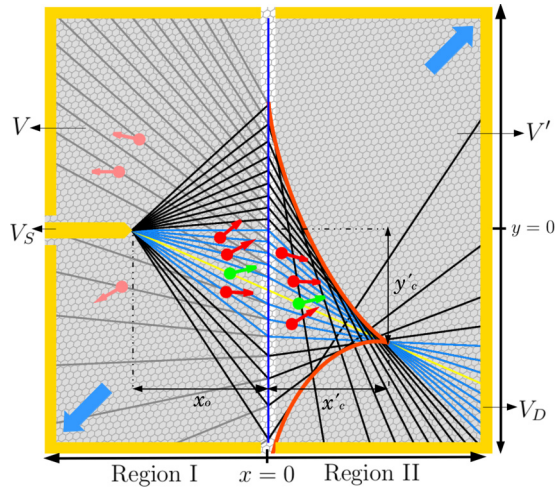

FIG. 5. Spherical-like aberration of asymmetric Veselago lenses. Distorted caustics with a common cusp are formed when the focusing condition is lifted. The cusp is located on the Klein tunneling path.

It is important to note that perfect tunneling occurs when electrons fly on the straight line which links the point source to the focus. Although the pseudospin and group velocity have different directions, the angles $\phi = -\alpha_x$ and $\theta = \theta_{KT}$ remain in the KT, as shown in Figs. 4(a), 4(b) and 4(d). Moreover, one part of the incoming particle flow has a positive refraction within the incidence range $0 \leqslant |\theta| \leqslant |\arctan(2\tan\theta_{KT})|$ [see Figs. 4(a), 4(b) and 4(c)]. Such positive refraction is caused by the rotation of the Dirac cones. This atypical result contrasts with the total negative refraction of conventional Veselago lenses [3,29,35]. The symmetrical case is recovered by applying uniaxial strain along the $\zeta = 0^\circ$ or 90° direction, as shown in Fig. 4(c). Another effect is the obtention of reflected electron beams staying on the same straight line as refracted electrons [see Figs. 4(a) and 4(b)]. From the optical laws (10), (11), (17), and (18) it can be verified that the propagation and pseudospin orientation of reflected and refracted electrons are opposite, namely, $\phi' = -\overline{\phi}$ and $\theta' = -\overline{\theta}$.

Asymmetrical charge densities on both sides of the homojunctions do not modify the angular deviation of KT, as shown in Fig. 5. In such situations it is known that caustics and cusps appear in VLs when the focusing condition lifts [3]. Likewise, finite temperature still causes a similar spherical-like aberration in superlenses for the symmetric step potential condition [3,36]. In the present work, these cases can be treated in the same way considering the most general Snell's law (see Appendix B)

$$\tan\theta' = \frac{ss'\rho(\tan\theta - \tan\theta_{KT})}{\rho'\sqrt{1+\left(1-\frac{\rho^2}{\rho'^2}\right)\left(\frac{w_x(\tan\theta-\tan\theta_{KT})}{w_y\sin(\alpha_x+\alpha_y)}\right)^2}} + \tan\theta_{KT}, \tag{19}$$

where the reflection law (17) remains unchanged. As expected, the symmetric case (18) is recovered under the focusing condition $\rho = \rho'$. Snell's law (19) allows us to evidence that a small deviation in the focusing condition leads to the formation of a pair of asymmetric caustics with a common cusp (see Fig. 5). These curves are obtained by applying the singularity condition $\partial_\theta y_{II} = 0$ to the ray equation in region II. Thus, the caustics are given by

$$y_{\text{caus}}(x) = (x - x_0)\tan\theta_{KT} \pm \frac{w_y}{w_x}\sin(\alpha_x+\alpha_y)\sqrt{\frac{\rho^2\left(x^{2/3} - x_c'^{2/3}\right)^3}{\rho'^2-\rho^2}}, \tag{20}$$

where the cusp is located at the point $x'_c = ss'\rho' x_0/\rho$ and $y'_c = (x'_c - x_0)\tan\theta_{KT}$ on the same straight line as the KT, as shown in Fig. 5. The relative refraction index ρ'/ρ does not depend on the strain for USG homojunctions. Therefore, the position of the cusp is affected only by the angular deviation of KT and lifting of the focusing condition. The sharpness of electron focusing in AVLs is decreased by finite temperature like in the unstrained case.

Since specific strain values in AVLs can improve the particle transmission [see Fig. 4(d)], the average of Fresnel-like coefficient (14) with regard to the angle of incidence θ

$$\langle T_{pn}\rangle = \frac{w_y\sin(\alpha_x+\alpha_y)\left[w_x^3 + w_x w_y^2\cos(2\alpha_x+2\alpha_y) + w_y\left(w_y^2 - w_x^2\right)\sin(\alpha_x+\alpha_y)\right]}{w_x^4 + w_y^4 + 2w_x^2w_y^2\cos(2\alpha_x+2\alpha_y)} \tag{21}$$

is obtained (see Appendix C). Thus, Fig. 6 shows the particle transmission efficiency as a function of strain parameters. In the range $-30^\circ \leqslant \zeta \leqslant 30^\circ$, the particle tunneling is higher than in the unstrained case when the tensile strain is increased. However, for strain values in the interval $\epsilon > 15\%$ and $45^\circ < \zeta < 75^\circ$ a decrease in the particle transmission efficiency is observed. This behavior is because the pseudospin is rotated by the strain, as seen in Fig. 4(b). Thus, a strong change in the pseudospin orientation causes the increasing of reflection probability.

V. FABRY-PÉROT OSCILLATIONS IN HOMOJUNCTIONS OF UNIAXIALLY STRAINED GRAPHENE

The scattering of anisotropic massless Dirac fermions in n-p-n homojunctions of USG is considered [see Fig. 7(a)]. In this system, regions I and III have the same negative doping level, and region II of width D is positively doped, where back gate V_B and top gate V_T control the Fermi level and potential barrier, respectively. The coherence length and mean free path must be larger than the device dimensions to guarantee ballistic transport [6,18,56]. Since the three regions are identically deformed, the Dirac cones have the same position in the reciprocal space. This feature leads to valley-independent refraction. In order to address the particle scattering problem the same wave function (12) is used. For region III, the wave function (13) is identically written by deleting the prime on the parameters. The wave function in region II is given by

$$|\Psi_{II}\rangle = \frac{1}{\sqrt{2}}t'\begin{pmatrix}1\\ s'e^{i\phi'}\end{pmatrix}e^{ixp'_x/\hbar} + \frac{1}{\sqrt{2}}r'\begin{pmatrix}1\\ -s'e^{-i\overline{\phi}'}\end{pmatrix}e^{-ix\overline{p}'_x/\hbar}, \tag{22}$$

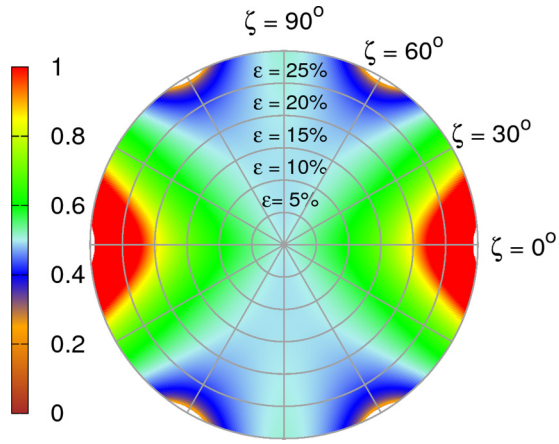

FIG. 6. Average transmission probability of the asymmetric Veselago lens as a function of uniaxial strain parameters ϵ and ζ. High transmission efficiency is found at the range $15\% \leqslant \epsilon \leqslant 28\%$ and $-30^\circ \leqslant \zeta \leqslant 30^\circ$. In contrast, low transmission probability occurs in the same range of ϵ and angular sector $45^\circ \leqslant \zeta \leqslant 75^\circ$.

where r' and t' are the amplitudes of the wave function within the potential barrier. Applying the matching conditions at $x = 0$ and $x = D$ and taking into account the novel electron optics laws of pseudospin (10) and (11), the transmission probability is

$$T_{npn}(\chi, \chi') = \frac{\cos^2\chi \cos^2\chi'}{\cos^2\chi \cos^2\chi' \cos^2\gamma + (1 - ss' \sin\chi \sin\chi')^2 \sin^2\gamma}, \tag{23}$$

where $\gamma = (w_y \rho' D/\hbar w_x)\cos\chi'$ shows the dependence of the resonant condition $\gamma = n\pi$ on the strain. This allows us to exhibit non-negligible changes in the interference pattern with regard to unstrained graphene transistors. In Figs. 7(b) and 7(c), the intraband ($s = s' = -1$) and interband ($s = -s' = 1$) tunneling regimes match perfectly due to the gapless band structure. This feature in the particle transmission density is due to the geometry of Dirac cones regardless of the pseudospin nature [19,57]. In this system, uniaxial tension along $\zeta \neq 0^\circ$ or 90° angularly shifts the KT and breaks the mirror symmetry of FP resonances, as shown in Figs. 7(b) and 7(c). It is possible to observe that anisotropic massless Dirac fermions have nonresonant tunneling when the angle of incidence is $\theta = \theta_{KT}$. In contrast, electrons impinging the barrier under normal incidence have nonzero backscattering probability

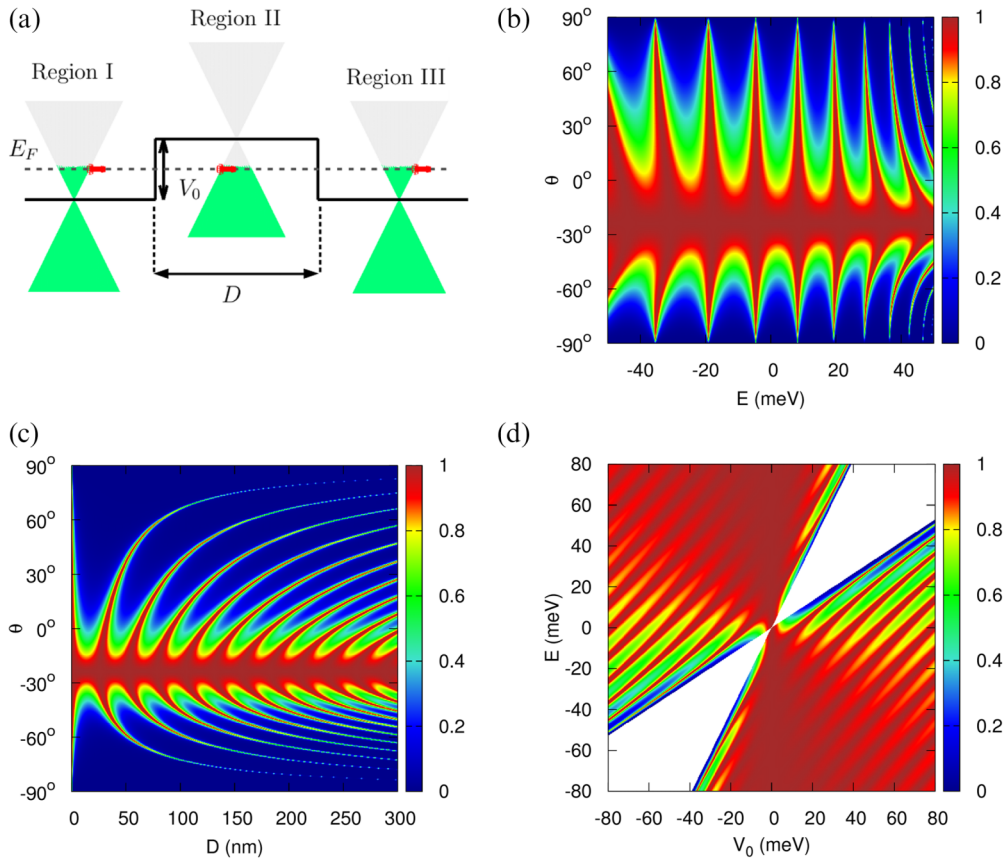

FIG. 7. Description of the particle scattering across an n-p-n homojunction of uniaxially strained graphene. (a) Schematic representation of the potential barrier and Dirac cone structure. Solid area represents the occupied states, and the horizontal dashed line shows the Fermi level. (b) Transmission probability as a function of θ and E for uniaxial strain values $\epsilon = 23\%$ and $\zeta = 45^\circ$. The barrier height is $V_0 = 100$ meV and width is $D = 100$ nm. (c) Transmission probability as a function of θ and D using the same set of strain values in (b) with $E = 50$ meV. The shifted Klein tunneling at $\theta_{KT} = -23.7^\circ$ remains unaffected against variations of E, D, and V_0. (d) Fabry-Pérot oscillations as a function of V_0 and E considering collimated electron beams under normal incidence and barrier width $D = 100$ nm. Total backscattering is observed for a specific range of E and V_0.

[see Fig. 7(d)]. This point shows a drastic difference with regard to the unstrained case. In graphene bipolar *n-p-n* junctions, incoming electron beams near normal incidence can cross the smooth potential barrier and present FP oscillations [20]. If sharp interface potentials are considered, electron beams with $\theta = 0$ perfectly cross the barrier without resonant tunneling regardless of the values of back gate V_B and top gate V_T [22]. In a USG transistor [see Fig. 7(d)], electrons impinging an abrupt potential barrier have FP oscillations when the Fermi level and height potential are tuned through the external gates V_B and V_T. The independence of E, V_0, and D in the perfect transmission is observed only for the deviated angle of incidence $\theta = \theta_{KT}$. Total backscattering of electrons under normal incidence emerges for a range of values of E and V_0 in Fig. 7(d). This occurs because the angle of normal incidence is greater than the critical angles,

$$\tan\theta_c^{\pm} = \tan\theta_{KT} \pm \frac{w_y \sin(\alpha_x + \alpha_y)}{w_x\sqrt{\rho^2/\rho'^2 - 1}}, \tag{24}$$

which are calculated from the refraction law (19). The gap transport appears in the range $c_+V_0 < E < c_-V_0$, where $c_\pm = 1/[1 \pm \cos(\alpha_x + \alpha_y)]$.

On the other hand, inhomogeneous strain features can modify the FP oscillations in graphene-extended *n-p-n* junctions. It is known that the effect of a position-dependent strain leads to the generation of pseudomagnetic fields [58]. However, the misalignment of Dirac cones causes the valley dependence in the refraction of electrons [44]. In graphene nanoribbon transistors, homogeneous strain effects on the FP resonances can be distinguishable from inhomogeneous strain patterns [58]. Both features may be mixed in extended transistor systems by the absence of gap transport. However, if collimated electron beams normally impinge on the potential barrier for values of E_F in the range $c_+V_0 < E < c_-V_0$ where total backscattering is predicted [see Fig. 7(d)], the influence of strain inhomogeneity on FP oscillations might be recognizable. On the one hand, the increasing of tensile strain makes the barrier for tension angles ζ near the normal direction transparent. This is because the pseudospin has a slow variation in θ. Thus, the deviated KT persists because the conservation of pseudospin is slightly affected for a wide incidence sector. The opposite case is observed for tension angles far away the normal axis. Again, electrons with $\theta = \theta_{KT}$ perfectly tunnel without deflecting their trajectory and regardless of the tunneling regime. However, the high angular variation rate of the pseudospin reduces the angular robustness of perfect transmission. Such observations in *n-p-n* homojunctions are similar to the behavior of the average transmission efficiency of AVLs through the tuning of strain parameters in Fig. 6.

VI. CONCLUSIONS AND FINAL REMARKS

In summary, partial positive refraction in asymmetrical Veselago lenses has been shown in uniaxially strained graphene homojunctions. The effective TB Weyl-like Hamiltonian was put forward to study the scattering of anisotropic massless Dirac fermions. These particles obey the atypical Fresnel-like coefficient and reflection and refraction laws which lead novel optical-like phenomena. Thus, electron rays under normal incidence have reflected and refracted beams different from zero. For uniaxial strains breaking the mirror symmetry with regard to the normal direction, Klein tunneling is angularly deviated. When the focusing condition is satisfied, the trajectory of perfect transmission occurs in the straight line that connects the point source and focus. Lifting this condition through the Fermi level modulation, the conservation of pseudospin guarantees the appearance of Klein tunneling. This effect persists in an *n-p-n* homojunction while varying the doping level, barrier width, and height. Fabry-Pérot interference shows asymmetrical resonant tunneling. In contrast to isotropic graphene, electrons under normal incidence can be backscattered. Further, uniaxial strain near the normal axis improves the particle transmission efficiency. This result could be used to avoid losses from draining in electron optics devices. Therefore, uniaxially strained graphene and related materials are good candidates for the realization of elliptical Dirac optics. The decrease in transmission efficiency by high tensile strains and tension angles far away from the normal axis could lead to the implementation of quantum confinement. Asymmetric Veselago lenses may be useful for the design of enhanced scanning tunneling microscopes with strain-bendable probing tips.

ACKNOWLEDGMENTS

Y.B.-O. gratefully acknowledges financial support from CONACYT Project "Fronteras 952 Transporte en sistemas pequeños, clásicos y cuánticos" and UNAM-DGAPA-PAPIIT, the Project No. IN-103017. The author also thanks T. Stegmann, F. Leyvraz, T. H. Seligman, G. Cordourier-Maruri, and R. de Coss for helpful discussions, comments, and critical reading of the manuscript.

APPENDIX A: COMPLEX VELOCITIES IN TERMS OF LATTICE VECTORS AND HOPPING PARAMETERS

In this Appendix we show the derivation of complex velocities in terms of lattice vectors and hopping parameters, which are obtained through a TB calculation to nearest neighbors. Using the definition of complex velocities in Eq. (8) and nearest-neighbor positions in terms of lattice vectors $\vec{a}_1$ and $\vec{a}_2$, we find that

$$w_x^c = \frac{i}{\hbar}\left(a_{1x}t_1 e^{-i\vec{K}_D\cdot\vec{\delta}_1} + a_{2x}t_2 e^{-i\vec{K}_D\cdot\vec{\delta}_2}\right), \tag{A1}$$

where w_y^c has an identical expression replacing $x \to y$. Taking into account the relation

$$\cos[\vec{K}_D\cdot(\vec{\delta}_1 - \vec{\delta}_2)] = \frac{t_3^2 - t_2^2 - t_1^2}{2t_1t_2}, \tag{A2}$$

which is obtained from the Dirac point equation $\sum_j^3 t_j e^{-i\vec{K}_D\cdot\vec{\delta}_j} = 0$, it is possible to prove that the square module of w_x^c given by

$$w_x^2 = \frac{1}{\hbar^2}\left[a_{1x}^2t_1^2 + a_{2x}^2t_2^2 + a_{1x}a_{2x}\left(t_3^2 - t_1^2 - t_2^2\right)\right] \tag{A3}$$

can be related to the strain parameters. Calculating $\mathrm{Im}\{w_x^{c*}w_y^c\}$, where the operations $\mathrm{Im}\{\cdot\}$ and * are the imaginary part and complex conjugate, respectively, a useful

identity of complex velocities and their phases

$$w_x^2 w_y^2 \sin^2(\alpha_x+\alpha_y) = \frac{1}{4\hbar^4}|\vec{a}_1\times\vec{a}_2|^2(t_1+t_2+t_3) \times(-t_1+t_2+t_3)(t_1-t_2+t_3)(t_1+t_2-t_3) \quad \text{(A4)}$$

is obtained. Such expressions serve to establish the bridge between complex velocities and uniaxial strain parameters from the relations (2) and (3) and exponential decay rule of t_j. In this way, the electron optics behavior in homojunctions of uniaxially strained graphene can be described.

APPENDIX B: DERIVATION OF ELECTRON OPTICAL LAWS IN ROTATED DIRAC CONE SYSTEMS

In order to obtain the electron optical laws in systems presenting rotated Dirac cones in their band structure, the conservation of E, p_y, and j_x must be applied. The definition of the pseudospin angle in the Weyl-like Hamiltonian (7) can be written in terms of linear momentum as

$$\tan\phi = \frac{-w_x p_x \sin\alpha_x + w_y p_y \sin\alpha_y}{w_x p_x \cos\alpha_x + w_y p_y \cos\alpha_y}. \quad \text{(B1)}$$

Using the dispersion relation

$$|E-V| = \sqrt{w_x^2 p_x^2 + w_y^2 p_y^2 + 2w_x w_y p_x p_y \cos(\alpha_x+\alpha_y)} \quad \text{(B2)}$$

and the effective Snell's law $p_y = \rho\sin\chi = \rho'\sin\chi'$, the x component in the linear momentum is given by

$$p_x = \pm\frac{w_y}{w_x}\rho\sin(\alpha_x+\alpha_y\mp s\chi), \quad \text{(B3)}$$

where $\rho = |E-V|/[w_y\sin(\alpha_x+\alpha_y)]$ is the effective refraction index. Substituting the linear momentum components in Eq. (B1), the relations of ϕ in Eq. (9) as a function of χ are found.

The optical laws of electron propagation are derived by determining the group velocity

$$v_x = \partial_{p_x}E = \frac{1}{s|E-V|}\left[w_x^2 p_x + w_x w_y p_y\cos(\alpha_x+\alpha_y)\right], \quad \text{(B4)}$$

where the dispersion relation (B2) of effective Weyl-like Hamiltonian (7) is considered. An identical expression for v_y is found, replacing $x\to y$ and $y\to x$. The direction of the electron beam in Eq. (15) is calculated by performing the ratio v_y/v_x and substituting the components of linear momentum in terms of χ for the cases of incidence, reflection, and refraction. It is possible to delete the dependence of χ in the reflection law (17) when the angles θ and $\bar{\theta}$ are related. In the electron refraction law for the AVLs (18) and (19), the χ dependence is removed using (15) to obtain θ' in terms of χ',

$$\tan\theta' = s'\frac{w_y}{w_x}\sin(\alpha_x+\alpha_y)\tan\chi' + \tan\theta_{KT}. \quad \text{(B5)}$$

Then, the effective Snell's law allows us to substitute χ' with χ. Applying inverse trigonometric properties yields

$$\tan\theta' = \frac{s' w_y\rho\sin(\alpha_x+\alpha_y)\sin\chi}{\rho' w_x\sqrt{1-\frac{\rho^2}{\rho'^2}\sin^2\chi}} + \tan\theta_{KT}. \quad \text{(B6)}$$

From Eq. (15), the relation of θ and χ is given by

$$\chi = \arctan\left(\frac{s w_x(\tan\theta-\tan\theta_{KT})}{w_y\sin(\alpha_x+\alpha_y)}\right). \quad \text{(B7)}$$

Therefore, the substitution of this last expression in Eq. (B6) leads to the general electron refraction law (19) and, using $\rho=\rho'$, to the Snell's law of AVLs (18).

APPENDIX C: AVERAGE FRESNEL-LIKE COEFFICIENT IN ASYMMETRIC VESELAGO LENSES

Since the transmission probability in AVLs is $T_{pn}(\chi) = \cos^2\chi$, the average of this quantity with regard to the angle of incidence θ is written as

$$\langle T_{pn}\rangle = \frac{1}{\pi}\int_{-\frac{\pi}{2}}^{\frac{\pi}{2}}\cos^2\chi\, d\theta. \quad \text{(C1)}$$

To integrate in χ it is necessary to use

$$\frac{d\theta}{d\chi} = \frac{w_x w_y\sin(\alpha_x+\alpha_y)}{w_x^2\cos^2\chi + w_y^2\cos^2(\chi-\alpha_x-\alpha_y)}, \quad \text{(C2)}$$

which is derived from expression (15). Using the defined integral [59]

$$\int_{-\frac{\pi}{2}}^{\frac{\pi}{2}}\frac{\cos^2\chi\, d\chi}{a\cos^2\chi + 2b\sin\chi\cos\chi + c\sin^2\chi} = \frac{\pi}{4b^2+(a-c)^2}\left[a-c+\frac{2b^2-(a-c)c}{\sqrt{ac-b^2}}\right], \quad \text{(C3)}$$

with parameters $a = w_x^2 + w_y^2\cos^2(\alpha_x+\alpha_y)$, $b = w_y^2\sin(\alpha_x+\alpha_y)\cos(\alpha_x+\alpha_y)$, and $c = w_y^2\sin^2(\alpha_x+\alpha_y)$, the expression for the average Fresnel-like coefficient in Eq. (21) is obtained, substituting the integral value in Eq. (C1).

[1] J. Spector, H. L. Stormer, K. W. Baldwin, L. N. Pfeiffer, and K. W. West, Appl. Phys. Lett. **56**, 1290 (1990).

[2] U. Sivan, M. Heiblum, C. P. Umbach, and H. Shtrikman, Phys. Rev. B **41**, 7937 (1990).

[3] V. V. Cheianov, V. Fal'ko, and B. L. Altshuler, Science **315**, 1252 (2007).

[4] J. L. Garcia-Pomar, A. Cortijo, and M. Nieto-Vesperinas, Phys. Rev. Lett. **100**, 236801 (2008).

[5] C. W. J. Beenakker, Rev. Mod. Phys. **80**, 1337 (2008).

[6] P. E. Allain and J. N. Fuchs, Eur. Phys. J. B **83**, 301 (2011).

[7] P. Rickhaus, P. Makk, M. H. Liu, K. Richter, and C. Schönenberger, Appl. Phys. Lett. **107**, 251901 (2015).

[8] P. Rickhaus, M. H. Liu, P. Makk, R. Maurand, S. Hess, S. Zihlmann, M. Weiss, K. Richter, and C. Schönenberger, Nano Lett. **15**, 5819 (2015).

[9] M. H. Liu, C. Gorini, and K. Richter, Phys. Rev. Lett. **118**, 066801 (2017).
[10] J. R. Williams, T. Low, M. S. Lundstrom, and C. M. Marcus, Nat. Nanotechnol. **6**, 222 (2011).
[11] R. D. Y. Hills, A. Kusmartseva, and F. V. Kusmartsev, Phys. Rev. B **95**, 214103 (2017).
[12] P. Boggild, J. M. Caridad, C. Stampfer, G. Calogero, N. R. Papior, and M. Brandbyge, Nat. Commun. **8**, 15783 (2017).
[13] C. Bäuerle, D. C. Glattli, T. Meunier, F. Portier, P. Roche, P. Roulleau, S. Takada, and X. Waintal, Rep. Prog. Phys. **81**, 056503 (2018).
[14] A. Weststrom and T. Ojanen, Phys. Rev. X **7**, 041026 (2017).
[15] M. A. Khan and M. N. Leuenberger, Phys. Rev. B **90**, 075439 (2014).
[16] D. Gunlycke and C. T. White, Phys. Rev. B **90**, 035452 (2014).
[17] C. H. Park, Y. W. Son, L. Yang, M. L. Cohen, and S. G. Louie, Nano Lett. **8**, 2920 (2008).
[18] V. V. Cheianov and V. I. Fal'ko, Phys. Rev. B **74**, 041403 (2006).
[19] Y. Betancur-Ocampo and V. Gupta, J. Phys.: Condens. Matter **30**, 035501 (2018).
[20] M. B. Shalom, M. J. Zhu, V. I. Fal'ko, A. Mishchenko, A. V. Kretinin, K. S. Novoselov, C. R. Woods, K. Watanabe, T. Taniguchi, A. K. Geim, and J. R. Prance, Nat. Phys. **12**, 318 (2016).
[21] C. Handschin, P. Makk, P. Rickhaus, M. H. Liu, K. Watanabe, T. Taniguchi, K. Richter, and C. Schönenberger, Nano Lett. **17**, 328 (2017).
[22] M. I. Katsnelson, K. S. Novoselov, and A. K. Geim, Nat. Phys. **2**, 620 (2006).
[23] B. Huard, J. A. Sulpizio, N. Stander, K. Todd, B. Yang, and D. Goldhaber-Gordon, Phys. Rev. Lett. **98**, 236803 (2007).
[24] A. V. Shytov, M. S. Rudner, and L. S. Levitov, Phys. Rev. Lett. **101**, 156804 (2008).
[25] R. Gorbachev, A. Mayorov, A. Savchenko, D. Horsell, and F. Guinea, Nano Lett. **8**, 1995 (2008).
[26] P. Rickhaus, R. Maurand, M. H. Liu, M. Weiss, K. Richter, and C. Schönenberger, Nat. Commun. **4**, 2342 (2013).
[27] N. Stander, B. Huard, and D. Goldhaber-Gordon, Phys. Rev. Lett. **102**, 026807 (2009).
[28] A. F. Young and P. Kim, Nat. Phys. **5**, 222 (2009).
[29] G. H. Lee, G. H. Park, and H. J. Lee, Nat. Phys. **11**, 925 (2015).
[30] S. Chen *et al.*, Science **353**, 1522 (2016).
[31] K. M. M. Habib, R. N. Sajjad, and A. W. Ghosh, Phys. Rev. Lett. **114**, 176801 (2015).
[32] A. A. Patel, N. Davies, V. Cheianov, and V. I. Fal'ko, Phys. Rev. B **86**, 081413 (2012).
[33] D. Schurig, J. J. Mock, B. J. Justice, S. A. Cummer, J. B. Pendry, A. F. Starr, and D. R. Smith, Science **314**, 977 (2010).
[34] V. G. Veselago, Sov. Phys. Usp. **10**, 509 (1968).
[35] J. B. Pendry, Phys. Rev. Lett. **85**, 3966 (2000).
[36] Y. Betancur-Ocampo, J. Phys.: Condens. Matter **30**, 435302 (2018).
[37] G. G. Naumis, S. Barraza-Lopez, M. Oliva-Leyva, and H. Terrones, Rep. Prog. Phys. **80**, 096501 (2017).
[38] M. Oliva-Leyva and G. G. Naumis, Phys. Rev. B **88**, 085430 (2013).
[39] V. M. Pereira, A. H. Castro Neto, and N. M. R. Peres, Phys. Rev. B **80**, 045401 (2009).
[40] V. M. Pereira and A. H. Castro Neto, Phys. Rev. Lett. **103**, 046801 (2009).
[41] Y. Betancur-Ocampo, M. E. Cifuentes-Quintal, G. Cordourier-Maruri, and R. de Coss, Ann. Phys. (NY) **359**, 243 (2015).
[42] T. Stegmann and N. Szpak, New J. Phys. **18**, 053016 (2016).
[43] Y. S. Ang, S. A. Yang, C. Zhang, Z. Ma, and L. K. Ang, Phys. Rev. B **96**, 245410 (2017).
[44] Z. Wu, F. Zhai, F. M. Peeters, H. Q. Xu, and K. Chang, Phys. Rev. Lett. **106**, 176802 (2011).
[45] Y. Jiang, T. Low, K. Chang, M. I. Katsnelson, and F. Guinea, Phys. Rev. Lett. **110**, 046601 (2013).
[46] M. M. Grujić, M. Z. Tadić, and F. M. Peeters, Phys. Rev. Lett. **113**, 046601 (2014).
[47] F. Zhai, Y. Ma, and K. Chang, New J. Phys. **13**, 083029 (2011).
[48] V. H. Nguyen, S. Dechamps, P. Dollfus, and J. C. Charlier, Phys. Rev. Lett. **117**, 247702 (2016).
[49] L. D. Landau and E. M. Lifshitz, *Theory of Elasticity*, 3rd ed. (Pergamon, Butterworth Heinemann, Oxford, 1986).
[50] L. Colombo and S. Giordano, Rep. Prog. Phys. **74**, 116501 (2011).
[51] E. Cadelano, P. L. Palla, S. Giordano, and L. Colombo, Phys. Rev. Lett. **102**, 235502 (2009).
[52] C. Lee, X. Wei, J. W. Kysar, and J. Hone, Science **321**, 385 (2008).
[53] A. H. Castro Neto, F. Guinea, N. M. R. Peres, K. S. Novoselov, and A. K. Geim, Rev. Mod. Phys. **81**, 109 (2009).
[54] D. A. Papaconstantopoulos, M. J. Mehl, S. C. Erwin, and M. R. Pederson, MRS Proc. **491**, 221 (1997).
[55] M. O. Goerbig, Rev. Mod. Phys. **83**, 1193 (2011).
[56] T. Low, S. Hong, J. Appenzeller, S. Datta, and M. S. Lundstrom, IEEE Trans. Electron Devices **56**, 1292 (2009).
[57] Y. Betancur-Ocampo, G. Cordourier-Maruri, V. Gupta, and R. de Coss, Phys. Rev. B **96**, 024304 (2017).
[58] D. A. Gradinar, M. Mucha-Kruczyński, H. Schomerus, and V. I. Fal'ko, Phys. Rev. Lett. **110**, 266801 (2013).
[59] I. S. Gradstheyn and I. M. Ryzhik, *Table of Integrals, Series, and Products*, 7th ed. (Academic, San Diego, 2007), p. 175.